aerospace

MDPI

Article

Space Environment Monitoring Unit on Wentian Laboratory Cabin Module of China Space Station

Huanxin Zhang [1,2,*], Guohong Shen [1,2], Donghui Hou [1,2], Shenyi Zhang [1,2], Chunqin Wang [1,2], Ying Sun [1,2], Liping Wang [1,2] and Jiajie Liao [1,2]

[1] National Space Science Center, Chinese Academy of Sciences, Beijing 100190, China
[2] Beijing Key Laboratory of Space Environment Exploration, Beijing 100190, China
* Correspondence: zhhx@nssc.ac.cn

Abstract: This article introduces the design and development of a space environment monitoring unit embedded in the versatile experimental assembly for electronic components outside the China space station's Wentian laboratory cabin module. A newly designed comprehensive detection system is being used for the first time in this kind of detector. The sensor head of the instrument includes a silicon telescope (composed of two silicon semiconductors) for measuring the LET spectrum and radiation dose rate, a typical chip for monitoring a single-event upset, and a CR-39 plastic nuclear track detector for detecting heavy ion tracks. The two silicon sensors stacked up and down are used for measuring the LET spectrum, which ranges from 0.001 to 100 MeV·cm^2/mg. A sensor charge allocation method is adopted to divide the detection range into four cascaded levels, each achieving different detection ranges separately and then concatenated together, while traditional detection methods need multiple sets of probes to achieve the same dynamic range. At the same time, using the two sensors mentioned above, the silicon absorption dose rate under two different shielding thicknesses can be obtained through calculation, ranging from 10^{-5} to 10^{-1} rad (Si)/h. Multiple calibration methods are applied on the ground. The preliminary in-orbit detection results are provided and compared with the simulation results obtained using the existing space environment model, and we analyze and discuss their differences.

Keywords: LET; dose rate; SEU; CR-39; China space station; heavy ion localization; space environment effect

Citation: Zhang, H.; Shen, G.; Hou, D.; Zhang, S.; Wang, C.; Sun, Y.; Wang, L.; Liao, J. Space Environment Monitoring Unit on Wentian Laboratory Cabin Module of China Space Station. *Aerospace* **2024**, *11*, 1006. https://doi.org/10.3390/aerospace11121006

Academic Editor: Jian Guo

Received: 9 October 2024
Revised: 16 November 2024
Accepted: 3 December 2024
Published: 5 December 2024

1. Introduction

The China space station (Tiangong space station) operates in a near-circular orbit with an altitude of 340–450 km and an inclination angle of 42°–43°. It is a long-term space infrastructure of on-orbit operations and is an important platform for conducting various space science experiments. With the completion of the construction of the China space station platform, more experiments, such as radiation biology experiments and life science experiments, have been continuously transferred from the ground to space. In order to ensure the safety of personnel and experimental equipment in orbit, the measurement of the space environment and quantifying its effects on the LEO have become more important. Single-Event Effects (SEEs) and total dose effects are the two most concerning space environment risks for uncrewed and crewed space operations, which seriously affect the reliability and lifespan of spacecraft and onboard equipment [1–5]. A large number of SRAM (Static Random-Access Memory), FPGA (Field-Programmable Gate Array), and other devices used on satellites are highly susceptible to single-particle flipping and locking caused by high-energy particles in space. The total dose effect on electronic parts and components includes the ionization effect and displacement effect, and MOS (Metal–Oxide–Semiconductor) devices have sensitivity to the ionization effect [6–8].

The versatile experimental assembly (VEA) arrived at the China space station aboard the Tianzhou-6 spacecraft on 10 May 2023, and it was installed outside the airlock cabin of

the Wentian cabin module. It mainly realizes the real-time in-orbit radiation environment monitoring and radiation resistance verification of various electronic components. The VEA operates in a composition mode of "platform + load". The platform part is composed of the mechanical structure of the testing device, the target adapter of the robotic arm, the active end of the load adapter, a central management control unit (CMCU), and a power supply and distribution unit (PSDU), and the load part is composed of a space environment monitoring unit (SEMU), a non-exposed area testing unit (NEU), and an exposed area testing unit (EU). The SEMU was developed by the National Space Science Center of the Chinese Academy of Sciences (NSSC). The installation position of the VEA is shown in Figure 1, in which "towards the sky" refers to the −Z direction. In a satellite fixed coordinate, "+X" points to the heading direction of the satellite, "+Z" points to the center of Earth, and "+Y" is determined by the right-hand rule.

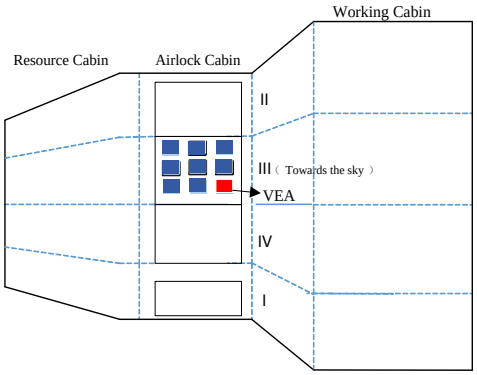

Figure 1. Installation of VEA on Wentian laboratory cabin module.

The SEMU is installed in the non-exposed area of the testing unit and connected to the CMCU and PSDU through a printed circuit board connector. The instrument is small in size, lightweight, and looks like a drawer, making it convenient for astronauts to install and remove.

The SEMU is mainly used for monitoring the space environment effects of the extravehicular components and modules on the space station. Through the SEMU, the linear energy transfer (LET) spectrum detection, radiation dose rate detection, and single-particle flipping probability detection of the orbit are achieved. These data can provide support for the analysis of the in-orbit radiation effects of components and improve ground simulation testing technology. A photo of the space environment monitoring unit is shown in Figure 2.

Figure 2. A photo of the space environment monitoring unit.

This article is organized as follows: Section 2 introduces the technical indicators of the SEMU. Section 3 describes the detector design, including the working principle and electronic design and particularly the application of the charge allocation method in wide-range LET spectrum measurement, introduced as a highlight. Section 4 discusses

the contents of calibration conditions and the testing results. Section 5 introduces the preliminary detection results in-orbit.

2. Technical Specifications

The main scientific objectives of the SEMU include the LET spectrum, the silicon absorption dose rate, single-event upset (SEU), and heavy ion track detection. The detailed detection indicators and engineering resource constraints are shown in Table 1.

Table 1. Main technical indicators of the SEMU.

No.	Parameter	Indicators	Notes
1	Silicon equivalent LET spectrum	0.001–100 MeV·cm^2/mg	64 channels
2	Silicon absorption dose rate	10^{-5}–10^{-1} rad (Si)/h	64 channels
3	Single-event upset	Data update rate: 1 s	Flip frequency and the address of the flipped register
4	Heavy ion track detection	/	Non-real-time
5	Overall dimension	175 × 260 × 80 mm	
6	Weight	2.5 ± 0.3 kg	
7	Power dissipation	≤6 W	

3. Instrument Design

3.1. Scheme of Detection System

The SEMU consists of a sensor system, electronic circuits, and a mechanical structure. The overall scheme design of the instrument is shown in Figure 3.

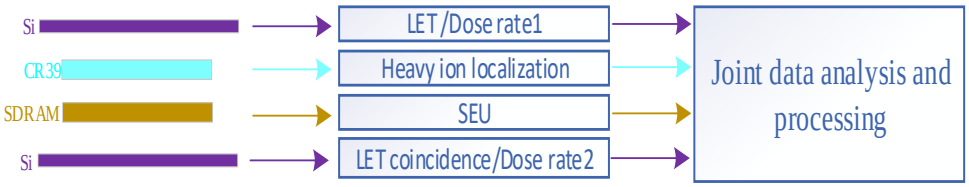

Figure 3. Block diagram of the overall design of the SEMU.

The sensor system includes two silicon semiconductors, an SDRAM chip, and a CR-39 solid-state track detector.

The silicon sensors are mainly used to measure the LET spectrum of the orbit, with an LET range of 0.001 to 100 MeV/(mg/cm^2), and to measure the radiation dose rate of 10^{-5} to 10^{-1} rad(Si)/h. The semiconductor sensors are circular with a diameter of 26 mm and a thickness of 300 μm, manufactured by Micro-Semiconductor, Brighton, UK.

A synchronous dynamic random access memory (SDRAM) is placed inside the instrument to test the single-particle event flipping probability of the memory. The model is IS42S16320B, with 512 M bits capacity (Integrated Silicon Solution Inc., Milpitas, CA, USA). This device was selected because it has a wide range of applications in ground equipment due to its large capacity and fast access speed, and its potential application in the aerospace field will be investigated. The SDRAM is set between the two semiconductor detectors. Combined with the in-orbit LET spectrum detection data, joint analysis can be carried out to obtain the correlation between the single-particle events and LET values [9,10].

The CR-39 plastic nuclear track detector is sensitive to high LET particles and is often used for measuring space radiation in the Chinese SJ-10 satellite [11]. In order to obtain the correspondence between the radiation LET spectrum and the SEU, a CR-39 detector (LANDAUER, Glenwood, IL, USA) is placed inside the instrument. It is mounted on the surface of the SDRAM chip, covering its sensitive area. Since the particle tracks are stored

in the CR-39 detector, after the detector returns to the Earth's surface with the cargo ship, it undergoes chemical etching with an etching solution, and then the particle information is read out by an optical microscope. Through track reconstruction and comparison, the type and energy of the incident particles can be obtained. This function is non-real-time and is a long-term evaluation of the heavy ion incident situation in the space station orbit. The integrated design of the CR-39 detector, the LET detector, and the single-particle flipping detector here is beneficial for studying the relationship between single-event upset and LET values [12].

The electronic circuits preprocess the electrical signals output by the sensor system and combine the collected data into a package and then communicate with the device bus to achieve data transmission. The hardware schematic diagram of the SEMU is shown in Figure 4.

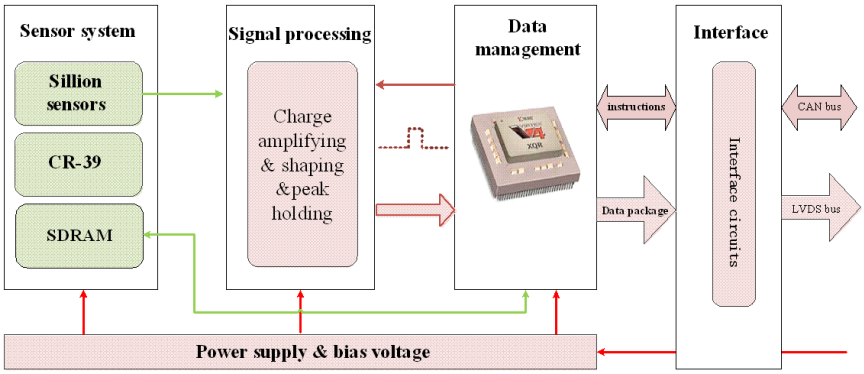

Figure 4. Electronic block diagram of the SEMU.

3.2. Silicon Equivalent LET Spectrum

The LET spectrum detection system adopts a telescope structure composed of two silicon sensors. When a particle hits the sensors, the deposited energy of the particle will cause ionization of the silicon sensors, resulting in the generation of electron–hole pairs. Under a bias voltage, electrons are collected at the input port of the charge-sensitive amplifier. After passing through the signal processing unit, the charge signal is converted into a pulse signal with a certain amplitude, and then it is sampled by an analog to digital conversion device (AD) in the data management unit. After a pulse amplitude analysis of the signals from both sensors, the equivalent LET spectrum and absorbed dose rate of particles in the silicon detector can be calculated. Figure 5 is a schematic diagram of the detection principle of the telescope system, in which the first sensor D1 detects the energy deposition of particles and the second sensor D2 is used to identify whether the particles go through the first sensor completely.

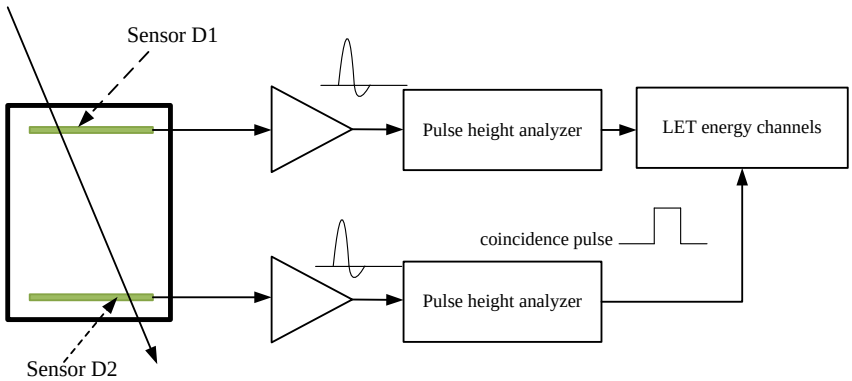

Figure 5. Schematic diagram of the detection principle of the LET spectrum.

In order to match the thickness of real silicon-based chips, the thickness of the silicon sensor should be as thin as possible. Considering the maturity of the production process for silicon sensors, a 300 μm silicon sensor is selected. The LET spectrum sensor is a silicon device, as is the SDRAM used in the SEU monitor. Therefore, the detected LET results can indirectly represent the LET values deposited in the SDRAM.

The equivalent particle radiation LET spectrum of a silicon sensor is defined as follows [13]:

$$\mathrm{LET(Si)} = \Delta E/\Delta d\ (\mathrm{keV}/\mu\mathrm{m}) \tag{1}$$

in which ΔE (keV) is the energy loss when a particle is incident into a silicon sensor, and Δd (μm) is the range of the particle in the sensor; here, Δd is the thickness of sensor D1. Therefore, only the deposited energy in the sensor ΔE needs to be measured.

The commonly used unit of LET is MeV·cm^2/mg, and

$$1\ \mathrm{keV}/\mu\mathrm{m}\ (\mathrm{Si}) = 4.31 \times 10^{-3}\ \mathrm{MeV}\cdot\mathrm{cm}^2/\mathrm{mg}\ (\mathrm{Si}) \tag{2}$$

The whole LET spectrum range is divided into 64 channels according to the logarithmic rule, and the particle LET value can be obtained by Equations (1) and (2):

$$\mathrm{LET}(i) = 10^{\log 70(\mathrm{keV}) + \frac{\log 6.9\times 10^6(\mathrm{keV}) - \log 70(\mathrm{keV})}{64}\times i} \times \frac{\mathrm{k}}{300(\mu\mathrm{m})}\left(\mathrm{MeV}\cdot\mathrm{cm}^2/\mathrm{mg}\right) \tag{3}$$

where i (0–63) denotes the channel number, the coefficient k is 4.31 × 10^{-3}, 300 μm is the thickness of the D1 sensor, and the number 64 represents the total number of channels.

According to the mission requirements, the detection range of the silicon equivalent LET spectrum is 0.001–100 MeV·cm^2/mg. Corresponding to a 300 μm silicon sensor, the detection range of the particle deposition energy is required to be 69.6 keV–6.96 GeV, and the corresponding charge amount is 3 fC–3 MfC, spanning 5 orders of magnitude, which will saturate any charge-sensitive amplifier.

In order to achieve such a measurement range, a charge allocation method is adopted for the output charge of the sensor, which divides the total charge into four parts and inputs them into independent preamplifiers. The basic principle is shown in Figure 6.

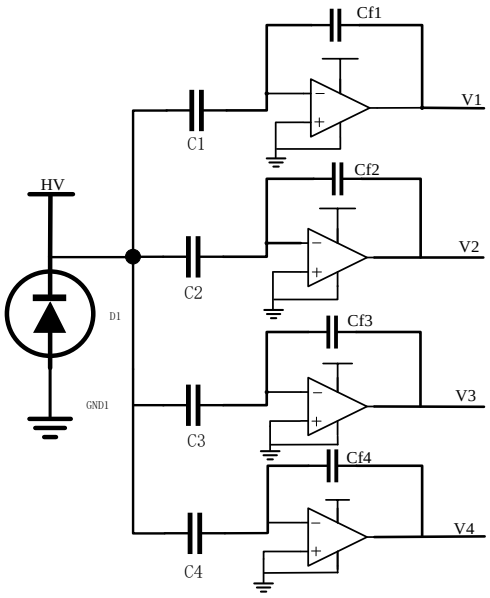

Figure 6. Schematic diagram of charge allocation circuit.

When a particle is incident into a sensor, the total charge generated through ionization in the sensor is Q, which is divided into Q1, Q2, Q3, and Q4 by the allocating capacitors

C1, C2, C3, and C4. Cf1–Cf4 are integral capacitors, which determine the gain of the charge-sensitive preamplifiers. The capacitance of each circuit is

$$C_{in} = \frac{C * (A * Cf)}{C + A * Cf} \approx C \quad (4)$$

in which A is the open-loop gain of the charge-sensitive preamplifier, and usually A is greater than 10^5. In the connection shown in Figure 6, the voltage at each input terminal is equal:

$$V_{in1} = V_{in2} = V_{in3} = V_{in4} \quad (5)$$

While

$$V_{in} = \frac{Q}{C_{in}} \quad (6)$$

So

$$\frac{Q1}{C1} = \frac{Q2}{C2} = \frac{Q3}{C3} = \frac{Q4}{C4} \quad (7)$$

The larger the allocating capacitor, the more charge is obtained for the circuit, and the output voltage is larger when the integral capacitors of each circuit are equal. According to this principle, the ratio of the allocating capacitor is set to C1:C2:C3:C4 = 8000:300:20:1, so that the output of the preamplifier is within the appropriate range of detection and the signal is not too small or too large.

Four independent processing circuits, each with different amplification gain, are adopted for signal processing. Therefore, the entire detection energy range is divided into four parts as shown in Table 2.

Table 2. Energy range corresponding to gain level.

Gain Level	Energy Range
High gain	65 keV–2.8 MeV
Medium-high gain	2.8 MeV–98 MeV
Medium-low gain	98 MeV–390 MeV
Low gain	390 MeV–7 GeV

The total energy detection range of the four processing circuits is 65 keV–7 GeV, and the equivalent LET spectrum measurement range in the 300 μm silicon semiconductor detector is 9.36×10^{-4} MeV·cm^2/mg–100.8 MeV·cm^2/mg.

3.3. Heavy Ion Track Detection

The CR-39 solid-state track detector is a relatively mature radiation detector developed in the 1960s [14–16], which has been widely used in fields such as individual dose monitoring, spacecraft radiation detection, and radiation biology research [17,18]. When heavy ions are incident on CR-39, they react with the CR-39 material, causing molecular bonds to break along its path, as well as complex secondary chemical processes such as the generation of free radicals and activators, which result in radiation damage to the material surrounding the ion's path and form a specific destructive region with reduced density. This damaged area forms the latent track of the particle. The characteristic size of latent tracks is related to the linear energy transfer (LET) value of charged particles, and their diameter generally ranges from a few nanometers to several tens of nanometers.

The CR-39 detector does not have signal decay issues and can be chemically etched with an etching solution after descending with the cargo ship and then read out by an optical microscope. Through track reconstruction and comparison, the LET values and deposition energy of incident particles can be obtained and used to analyze the types and energies of incident particles.

The CR-39 solid-state track detector has a positioning accuracy of nm for heavy ion detection. Considering the influence of the etching process, its positioning accuracy can also reach the micrometer level after etching.

3.4. Dose Rate Detection

According to the definition of the silicon absorption dose rate, it is known that the silicon absorption dose rate is the ratio of the total deposition energy of all types of radiation in silicon per unit of time to the mass of the silicon detector, as follows [13]:

$$D_{Si}(t) = \Delta E(t)/\Delta m \tag{8}$$

where $\Delta E(t)$ is the deposited energy of particles through ionizing radiation in the sensitive area of the silicon detector per unit of time, in joule (J), and Δm is the mass of the sensitive area of the detector, in kilograms (kg).

As mentioned above, this project uses a circular silicon sensor with a diameter of 26 mm and a thickness of 300 μm, so the mass of the sensitive area of the detector is 3.7×10^{-4} kg and only the total deposited energy $\Delta E(t)$ in the detector per unit time needs to be monitored to calculate the silicon absorption dose rate. Using the deposited energy obtained from detectors D1 and D2, the dose rate at the positions of the two sensors can be directly calculated.

3.5. Single-Particle Event Detection

In order to detect the probability of single-event upset, a single-event upset detector is placed between two silicon semiconductor sensors in the LET spectrum detector. The testing device is an ISSI SDRAM chip, model IS42S16320B.

The SDRAM chip is mainly composed of a storage core, a data input/output buffer, a row/column address latch, a frame counter, a cache and decoder, an instruction decoding and clock generator, a mode register, and BANK control logic modules. The SEMU uses the SDRAM storage core as an auxiliary testing device and accesses the stored data in SDRAM through the FPGA loop, then makes judgments by comparing it with preset values. If the data are consistent, it is determined that no single-particle event has occurred; otherwise, the location and status data of a single-particle event are recorded. Figure 7 shows the internal structure of the SDRAM chip [19].

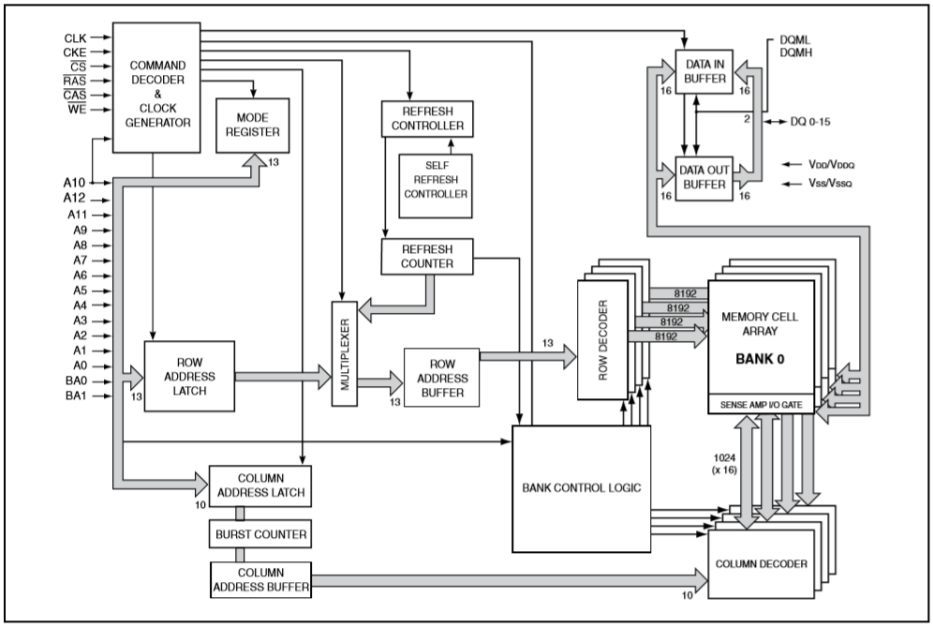

Figure 7. Schematic diagram of internal structure of the SDRAM.

4. Calibration

4.1. Calibration Conditions

Both the LET spectrum measurement and silicon absorption dose rate measurement are based on the collection and analysis of the number of charges generated by the ionization of particles incident on two silicon sensors. Then, the LET spectrum and silicon absorption dose rate are calculated based on Formulas (1) and (8). Therefore, the calibration focuses on the response of the electronic circuits to charges generated by particles incident on the sensor, including the energy resolution, linearity, and energy range.

Due to the limitation of particle beam energy, multiple calibration methods were adopted, as shown in Table 3.

Table 3. Calibration methods used for the SEMU.

Calibration Methods	Source Type	Energies Used for Calibration
Electron accelerator (NSSC)	electron	Multiple energies between 69 keV and 500 keV
Proton and heavy ion accelerator (China Institute of Atomic Energy)	proton	10 MeV, 15 MeV
	Li	40 MeV, 46 MeV
	O	80 MeV, 100 MeV
Radioactive source Am241 (NSSC)	alpha	5.48 MeV

4.1.1. Energy Linearity

The accelerator calibration cannot cover all the energy ranges, so it is necessary to calibrate the linearity of the energy response in order to extrapolate based on this.

The basic principle of energy linearity calibration is that the energy loss of particles in a silicon detector is theoretically strictly proportional to the amplitude of the output pulse signal. Assuming that the energy deposition of particles in a sensor is ΔE (MeV), then the number of electron–hole pairs generated by the energy loss of E in the silicon detector N = ΔE/3.62, and the generated charge Q = N × 1.62 × 10^{-19} (Coulomb), then the relationship between the energy loss and the pulse signal is obtained as follows:

$$U(v) = \frac{\frac{\Delta E(eV)}{3.62} \times 1.6 \times 10^{-19}}{C(F)} \tag{9}$$

in which $U(v)$ is the voltage value output by the charge amplifier in the signal processing unit and $C(F)$ is the integral capacitance of the amplifier.

By conducting accelerator tests on five or more energy points, a linear relationship between the deposited energy and the voltage output can be fitted, thereby determining the response of all energy points.

4.1.2. Energy Resolution

The energy deposition spectrum of particles in sensors is approximately a Gaussian distribution. In particle physics, the definition of energy resolution is defined as follows:

$$\eta = \frac{\text{FWHM}}{\lambda_0} \times 100\% \tag{10}$$

where λ_0 is the deposited energy and the FWHM (full width at half maximum) is the energy broadening width at half of the peak height derived from the Gaussian fitting curve. See Figure 8.

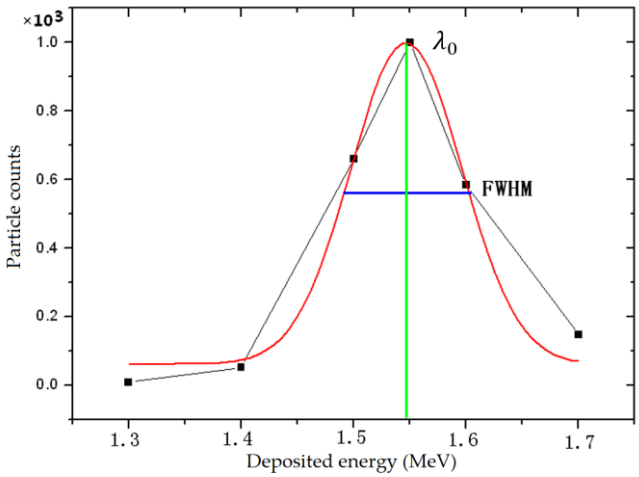

Figure 8. Definition of energy resolution.

4.2. Calibration Results

4.2.1. Energy Resolution and Linearity

Using the 200 keV and 2 MeV accelerators of the "Space Payload Test and Calibration Platform" of the Chinese Academy of Sciences, as well as the proton and heavy ion accelerator of the China Institute of Atomic Energy (CIAE), the two silicon sensors and their four-stage processing circuits with different gains underwent abundant accelerator calibration. Due to the limitation of particle energy in accelerators, analog signal sources were used instead of particle sources for low-gain and medium-low-gain amplification circuits. The response of typical energy points and their Gaussian fitting results are shown in Figure 9.

According to the testing data of the Gaussian peak position corresponding to the deposited energy, the energy linearity is obtained by linearly fitting these peak positions, as shown in Figure 10.

We performed the energy calibration with all the gain levels for both sensor D1 and D2. According to the calibration results, the energy linearity and energy resolution are shown in Table 4.

Table 4. Calibration results of energy linearity error and energy resolution.

Sensor	Amplification Gain Channel	Energy Resolution	Linearity Error
D1	High gain	8.95%	3.81%
	Medium-high gain	0.84%	2.65%
	Medium-low gain	0.92%	2.30%
	Low gain	0.45%	4.73%
D2	High gain	7.35%	1.17%
	Medium-high gain	0.46%	5.73%
	Medium-low gain	3.62%	0.46%
	Low gain	2.67%	5.53%

4.2.2. Detection Range of LET Spectrum and Dose Rate

Based on the energy linearity calibration, the actual energy range detected can be obtained by linear extrapolation, which is 69.1 keV–6963 MeV for sensor D1. According to the calculation formula of the LET spectrum, the measurement range of the LET spectrum is 9.93×10^{-4}–100.04 (MeV·cm^2/mg).

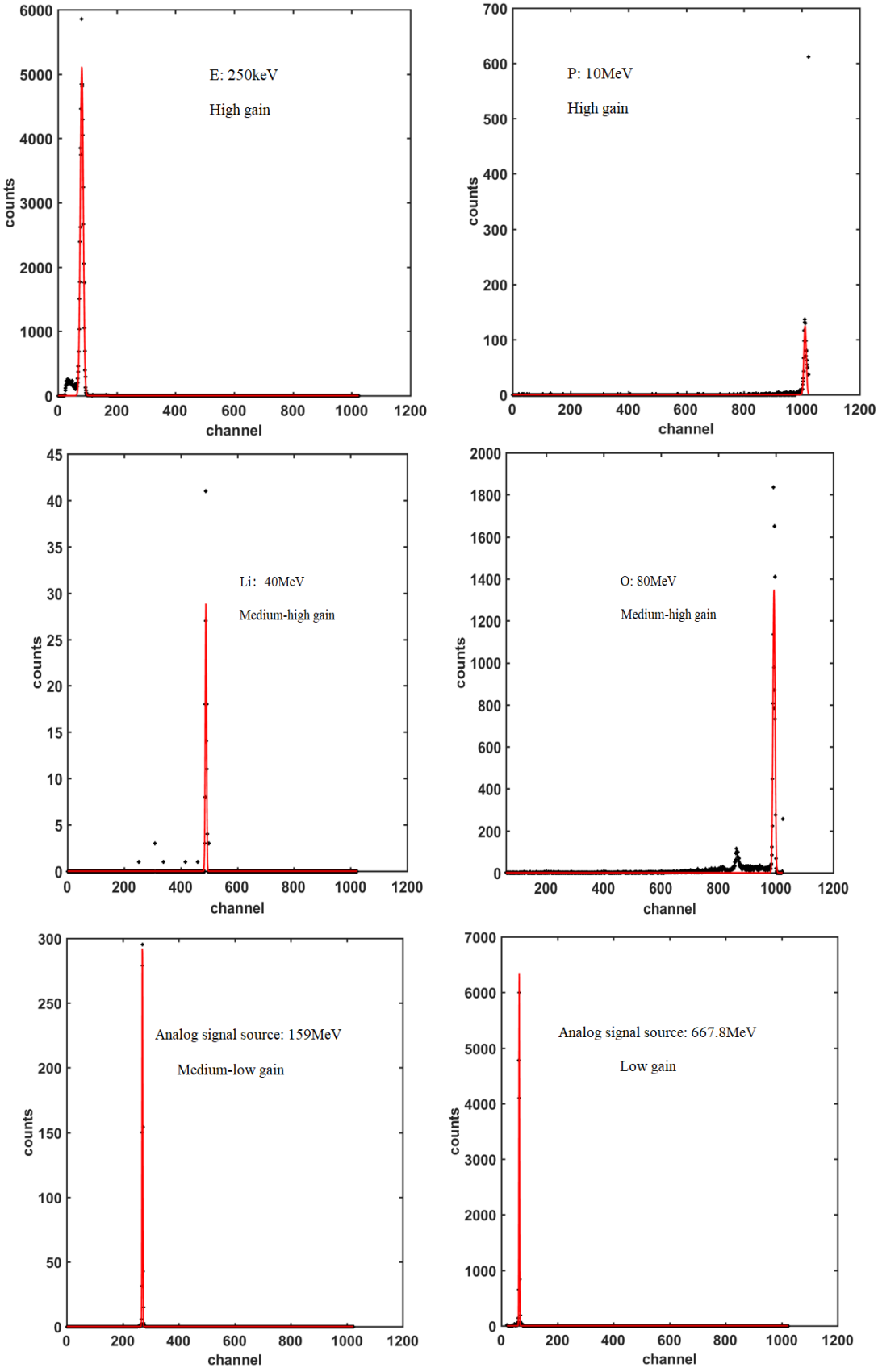

Figure 9. Calibration data (black points) and Gaussian fitting curve (red).

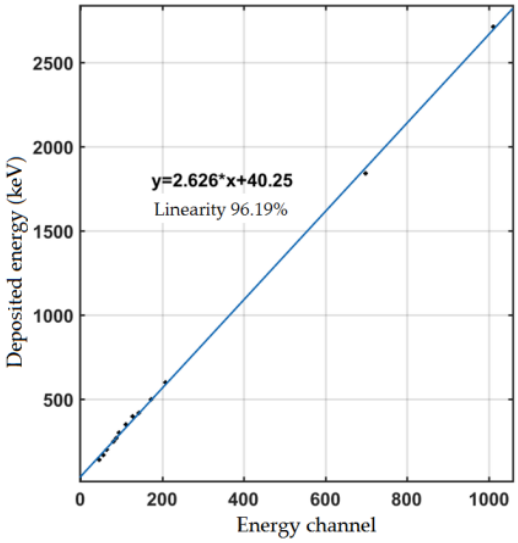

Figure 10. The energy linearity at high gain.

For the dose rate, there are no standard calibration specifications applicable to this type of dose detector, nor are there standard particle beams used for calibration. It is not only related to the deposited energy of particles, but also related to the time period and the mass of the medium. Here, we use the calibrated deposited energy and simulated in-orbit incident particle energy spectrum to estimate the range of radiation dose rate. The space environment simulation is based on two extreme situations of the orbital environments. When the space station is located outside the radiation belt and there are only galactic cosmic rays, the dose rate is considered to be the minimum value. When the space station is located in the worst-case space environment of the South Atlantic anomaly (SAA) area, the dose rate is supposed to be the maximum. The absorbed dose rate can be used to represent the radiation energy absorbed by a medium per unit of time and mass after the sensor is irradiated by radiation. Therefore, the absorbed dose rate of particles in the medium is $(1.602 \times 10^{-7}\ \Delta E)/\Delta M$, where ΔE is the deposited energy per unit time (in keV/s), ΔM is the mass of the sensor (in grams), and the absorbed dose rate is in the unit of μGy/h.

The final obtained LET spectrum and dose rate range are shown in Table 5.

Table 5. Dose rate and LET spectrum measurement range.

Parameter	Detection Range	Note
Dose rate (D1)	7.48×10^{-6}–1.6×10^{-1} rad/h (Si)	Equivalent shielding 4.2 mm
Dose rate (D2)	4.54×10^{-6}–10^{-1} rad/h (Si)	Equivalent shielding 7.5 mm
LET	9.93×10^{-4}–100.04 MeV/(mg/cm^2)	

5. Data Obtained in Orbit

Figures 11 and 12 show the spatial distribution of the radiation dose rate data obtained by the SEMU from the two sensors D1 and D2 for 3 days (29 December 2023–1 January 2024). The significant irradiation effect of the orbital space is reflected in the anomalous area of the South Atlantic in the inner radiation belt region. The equivalent shielding of sensor D1 is smaller than that of sensor D2, so its radiation dose rate is higher than that of sensor D2.

The dose values of the orbit under different shielding thicknesses calculated by the AP8/AE8 model within one year are shown in Figure 13.

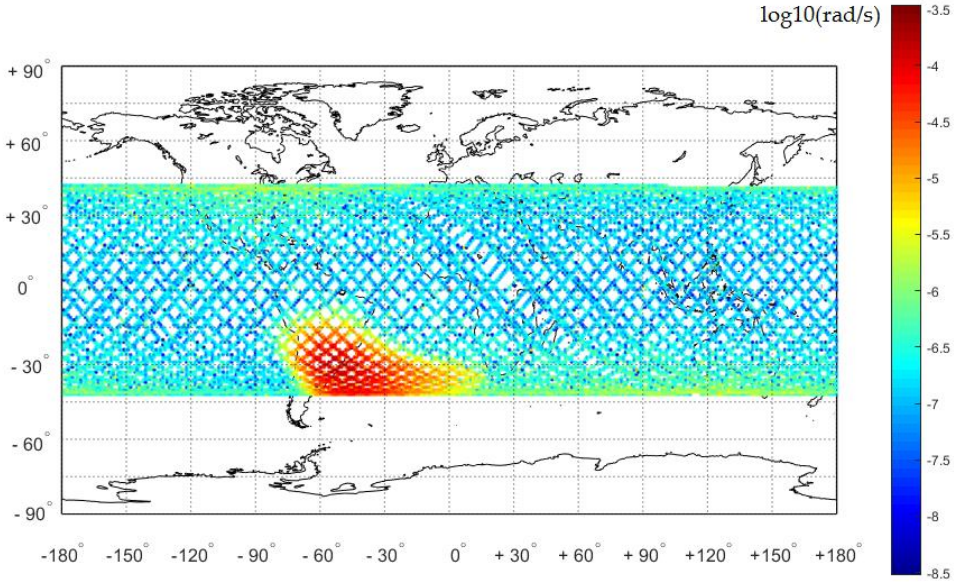

Figure 11. Spatial distribution of SEMU-D1 radiation dose (3 days of dose).

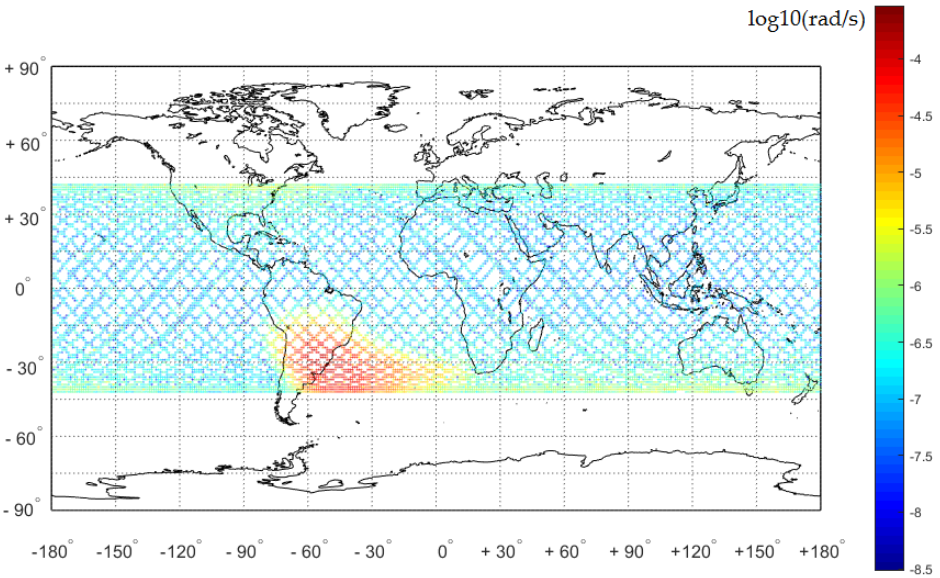

Figure 12. Spatial distribution of SEMU-D2 radiation dose (3 days of dose).

Table 6 provides preliminary statistical values for the radiation dose rates from SEMU/D1 and D2 and the result from the AP8/AE8 model. It can be seen that the radiation dose of D1 is 1.3 times more than the radiation dose of D2, and the measured value is about one-third of the average dose value calculated by the model under the same shielding. One reason for that is that the field of view is slightly obstructed by the adapter, which is located above the side of the VEA; the other reason is that it is in a quiet space environment during in-orbit measurement.

Figure 14 shows the LET spectrum obtained in 5 days (27 December 2023–1 January 2024) and LET values calculated by the AP8/AE8 model. It can be seen that the measured LET spectrum is an approximate power law distribution, and it is lower than the model-calculated value at the low end, while at the high end, particles with LET values greater than 3 MeV·cm^2/mg were detected. The LET values detected in orbit currently do not cover five orders of magnitude, as the occurrence of particles with high LET values (mainly from cosmic rays) in this orbit is a low-probability event.

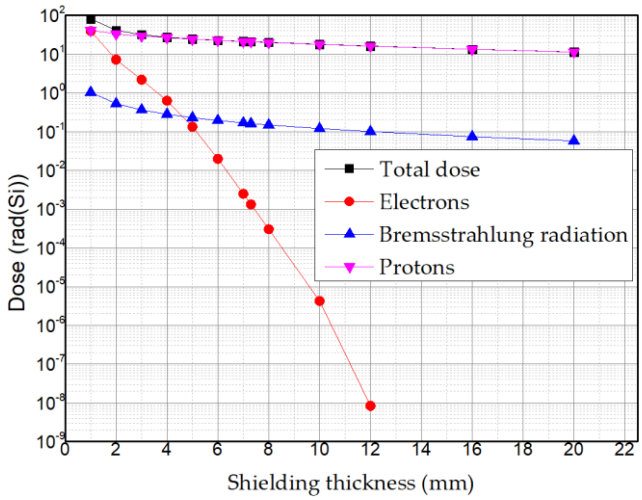

Figure 13. Dose calculated by AP8/AE8 semi-infinite model (for 1 year).

Table 6. Preliminary results of radiation dose rate.

Detector	Measured Average Dose Rate rad(Si)/s	Measured Peak Dose Rate rad(Si)/s	Daily Cumulative Dose rad(Si)/Day
SEMU-D1 (4.2 mm)	9.36×10^{-4}	3.3×10^{-5}	0.022
SEMU-D2 (7.5 mm)	7.2×10^{-4}	2.5×10^{-5}	0.017
AP8/AE8 Model (4.2 mm)	2.83×10^{-3}	/	0.068
AP8/AE8 Model (7.5 mm)	2.35×10^{-3}	/	0.056

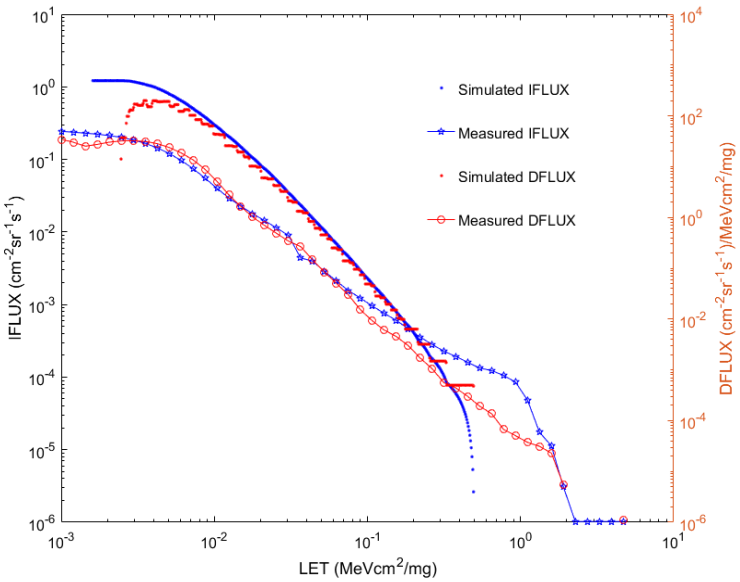

Figure 14. Comparison of in-orbit LET results and simulated data by model.

6. Conclusions

The space environment monitoring unit carried by the versatile experimental assembly of the China space station uses a comprehensive sensor system and its electronic circuits. By adopting a charge allocation method, a large dynamic range measurement of the LET spectrum spanning five orders of magnitude from 0.001 MeV·cm^2/mg to 100 MeV·cm^2/mg was achieved. At the same time, the detector was used to obtain radiation dose rates under

two different types of shielding. The ground calibration shows that the design can meet the requirements of detection indicators. The LET spectrum and dose rate obtained in orbit were compared with space environment simulations, and due to structural obstruction of the field of view, the measured dose rate and the flux of the low LET values are lower than the simulated results. Particles with high LET values (>3 MeV·cm^2/mg) were detected. The data of a single-event upset are continuously accumulating, and the heavy ion detection data of the CR-39 solid-state track detector needs to be processed after the detector returns to the ground. These detection results will be further studied in subsequent work, and a joint data analysis will continue to serve the long-term operation of the China space station.

Author Contributions: Conceptualization, H.Z.; funding acquisition, G.S.; project administration, H.Z. and S.Z.; data curation, C.W. and D.H.; resources, Y.S. and L.W.; writing—original draft preparation, H.Z. and J.L. All authors have read and agreed to the published version of the manuscript.

Funding: This research received no external funding.

Data Availability Statement: The data presented in this study are available on request from the corresponding author.

Acknowledgments: We thank the following facilities and personnel for supporting the calibration of SEMU: the NSSC-SEF (National Space Science Center-Space Electron Facility), China; the irradiation facility dedicated to heavy-ion-induced single-event effects, CIAE (China Institute of Atomic Energy), China; and the HIRFL Heavy Ion Research Facility in Lanzhou, China. We thank Gang Guo/CIAE and Jie Liu/HIRFL for providing calibration services.

Conflicts of Interest: The authors declare no conflicts of interest.

References

1. Van Allen, J.A. Radiation Belts Around the Earth. *Sci. Am.* **1959**, *200*, 39–47. [CrossRef]
2. Jiao, W.X.; Pu, Z.Y.; Fang, X.H.; Fu, S.Y. Radiation environment in the geomagnetic anomaly area of the South Atlantic and the calculation of particle radiation flux of low-orbit satellites. *Chin. J. Geophys.* **1999**, *2*, 163–168.
3. Cucinotta, F.A. Space radiation risks for astronauts on multiple International Space Station missions. *PLoS ONE* **2017**, *9*, e96099. [CrossRef] [PubMed]
4. Dietze, G.; Bartlett, D.T.; Cool, D.A.; Cucinotta, F.A.; Jia, X.; McAulay, I.R.; Pelliccioni, M.; Petrov, V.; Reitz, G.; Sato, T. ICRP Publication 123: Assessment of Radiation Exposure of Astronauts in Space. *Ann. ICRP* **2013**, *42*, 1–339. [CrossRef] [PubMed]
5. Cheng, P.C.; Min, R. An overview of near-earth space radiation and its protection. *Radiat. Prot. Bull.* **2017**, *37*, 14–21.
6. Xue, Y.X.; Yang, S.S.; Ba, D.S.; An, H.; Liu, Q.; Shi, H.; Cao, Z. Analyze of spacecraft system failures and anomalies attributed to the natural space radiation environment. *Vac. Cryog.* **2012**, *18*, 63–70.
7. Wang, T.Q.; Shen, Y.P.; Wang, S.W.; Zhang, S.F. Radiation effects in space radiation environment. *J. Natl. Univ. Def. Technol.* **1999**, *21*, 36–39.
8. Pu, J.; Ye, Z.H. Effects of space particle radiation on integrated chips in satellites. *Chin. J. Space Sci.* **1993**, *13*, 292–298. [CrossRef]
9. Sajid, M.; Chechenin, N.G.; Torres, F.S.; Gulzari, U.A.; Butt, M.U.; Ming, Z.; Khan, E.U. Single Event Upset rate determination for 65 nm SRAM bit-cell in LEO radiation environments. *Microelectron. Reliab.* **2017**, *78*, 11–16. [CrossRef]
10. Wu, Z.; Chen, S.; Yu, J.; Chen, J.; Huang, P.; Song, R. Recoil-ion induced single event upsets in nanometer cmos sram under low-energy proton radiation. *IEEE Trans. Nucl. Sci.* **2017**, *64*, 654–664. [CrossRef]
11. Zhou, D.; Zhang, B.; Zhang, S.; Sun, Y.; Liang, J.; Zhu, G.; Jing, T.; Yuan, B.; Zhang, H.; Zhang, M.; et al. Radiation Measured for Chinese Satellite SJ-10 Space Mission. *J. Geophys. Res. Space Phys.* **2018**, *123*, 1690–1700. [CrossRef]
12. Zhang, B.; Zhang, S.; Shen, G.; Tuo, C.; Zhang, X.; Zhang, H.; Quan, L.; Tian, C.; Hou, D.; Zhou, P.; et al. Monitor of the single event upsets and linear energy transfer of space radiation on the Beidou navigation satellites. *Open Astron.* **2023**, *32*, 20220206. [CrossRef]
13. Sun, L.; Li, S.J. *Fundamentals of Ionizing Radiation Dosimetry*; China Atomic Energy Press: Beijing, China, 2014.
14. Benton, E.V.; Henke, R.P. Heavy particle range-energy relations for dielectric nuclear track detectors. *Nucl. Instrum. Methods* **1969**, *67*, 87–92. [CrossRef]
15. Bücker, H.; Horneck, G. Biological effectiveness of HZE-particles of cosmic radiation studied in Apollo-16 and Apollo-17 biostack experiments. *Acta Astronaut.* **1975**, *2*, 247–264. [CrossRef] [PubMed]
16. Curtis, S.B. Single track effects, biostack and risk assessment. *Radiat. Meas.* **1994**, *23*, 5–8. [CrossRef] [PubMed]
17. Gao, M.; Zhao, G.H.; Gu, Y.D. Space science and application mission in China's space station. *Bull. Chin. Acad. Sci.* **2015**, *30*, 721–732.

18. Liu, J.; Shi, Y.; Cui, Y.T.; Hou, J.; Zhang, K.; Huang, A.J. Research progress and prospect of on-orbit additive manufacturing technology. *Chin. Space Sci. Technol.* **2022**, *42*, 23–34.
19. Integrated Silicon Solution, Inc. IS42S16320B Datasheet. Available online: www.issi.com (accessed on 3 May 2021).